Anisotropy of the electron momentum density of graphite studied by $(\gamma,e\gamma)$ and $(e,2e)$ spectroscopy

T. Sattler, Th. Tschentscher, and J. R. Schneider
Hamburger Synchrotronstrahlungslabor (HASYLAB) at Deutsches Elektronen-Synchrotron (DESY), Notkestraße 85, 22603 Hamburg, Germany

M. Vos, A. S. Kheifets, D. R. Lun, and E. Weigold
Atomic and Molecular Physics Laboratory, Research School of Physical Sciences and Engineering, The Australian National University, Canberra ACT 0200, Australia

G. Dollinger
Physik-Department E 12, Technische Universität München, 85747 Garching, Germany

H. Bross
Sektion Physik, Ludwig-Maximilians-Universität München, Theresienstraße 37, 80333 München, Germany

F. Bell
Sektion Physik, Ludwig-Maximilians-Universität München, Am Coulombwall 1, 85748 Garching, Germany
(Received 6 June 2000; published 30 March 2001)

The electron momentum density (EMD) of two different modifications of graphite has been measured and the results of the measurements have been compared with theoretical calculations from three different theories: a full potential linear muffin-tin orbital, a modified augmented plane wave, and a pseudopotential calculation. Experimental results have been obtained by two different methods. The complete three-dimensional EMD is determined by inelastic photon-electron scattering, i.e., by the so-called $(\gamma,e\gamma)$ experiment, and by electron-electron scattering, the $(e,2e)$ experiment, cuts in the spectral electron momentum density are studied. For the $(\gamma,e\gamma)$ experiment 180 keV synchrotron radiation from the PETRA storage ring at the Deutsches Elektronen-Synchrotron has been used with coincident detection of the recoil electrons. The $(e,2e)$ experiments were carried out at the new $(e,2e)$ spectrometer at the Australian National University using 40 keV primary electron energy and simultaneous detection of the outgoing electrons in an equal energy sharing mode. As samples we have prepared approximately 20 nm thin self-supporting graphite foils either by thermal evaporation (TE) or by laser plasma ablation (LPA). They are thin enough to suppress in essence electron multiple scattering. Electron diffraction analysis revealed that the LPA foil contains graphitic basal planes with a random distribution of *c* axes, whereas the TE foil was strongly *c*-axis oriented in the sense that the basal planes were parallel to the foil surface. In the analysis of the results special attention was devoted to anisotropies in the EMD revealed by comparison of TE and LPA foils. The $(e,2e)$ measurements showed furthermore a strong orientation dependence of the intensity of π and σ states (here we have for comparison additionally measured highly oriented pyrolytic graphite). The EMD's obtained by both techniques show anisotropies in the momentum distribution of graphite and are discussed in view of the theoretical results.

DOI: 10.1103/PhysRevB.63.155204 PACS number(s): 71.20.Mq, 32.80.Cy, 78.70.Ck, 82.80.Pv

I. INTRODUCTION

Graphite is the prototype of a layered material with exceptionally strong sp^2 covalent intralayer bonding and weak van der Waals interlayer bonding. This highly anisotropic bonding gives rise to a number of unusual properties that are of long-standing technological and scientific importance.[1] Especially the band structure (BS) of graphite has been the subject of both theoretical[2] and experimental studies. Energy dispersion of the valence states has been investigated either for the occupied states by angle-resolved photoelectron spectroscopy (ARPES) (Refs. 3–5) or by inverse photoemission spectroscopy (ARIPES) in case of unoccupied states.[6,7] In addition, inelastic x-ray scattering, both resonant[8] and nonresonant,[9] electron-energy-loss spectroscopy (EELS),[10,11] or angle-resolved x-ray fluorescence and absorption spectroscopy[12]—to name just a few methods—mainly concern the energetics of the band structure. In contrast, information about wave-function-related quantities such as electron densities[13] or electron momentum densities (EMD's) is rather scarce. EMD's have mainly been investigated by positron-annihilation experiments (ACAR) (Refs. 14,15) or by Compton scattering using either a photon or an electron as projectile. The Doppler broadening of the scattered projectile intensity has either been measured in a noncoincident fashion yielding the so-called Compton profile or in a coincident mode, i.e., simultaneously with the recoil electron. In the latter case, scattering kinematics are fixed and allow the complete reconstruction of the initial electron momentum yielding the three-dimensional (3D)-EMD in contrast to the 1D information of the Compton profile.

Anisotropies of graphite by noncoincident photon scatter-

 ©2001 The American Physical Society

ing have been obtained by Manninen *et al.*[16] They clearly show the influence of π states which are responsible for the interlayer bonding. Due to their p character, Compton profiles along the c axis of graphite are smaller at low momenta than profiles in the basal plane. Electron Compton profiles have been measured either in the noncoincident mode[17,18] or 3D-EMD's by fixing the kinematics in a so-called $(e,2e)$ experiment.[19–21] In the photon scattering analogy $(\gamma,e\gamma)$, the scattered photon is measured simultaneously with its recoil electron.[22,23] Although all three methods, i.e., ACAR, $(e,2e)$, and $(\gamma,e\gamma)$ measure EMD-related phenomena, each has its own advantages and drawbacks. Strictly speaking, ACAR does not measure EMD's but the electron-positron pair density, i.e., the momentum density weighted by the positron wave function. It is for this reason that ACAR is mainly used to investigate Fermi breaks (Fermiology) provided they exist.[24]

A major problem for both $(e,2e)$ and $(\gamma,e\gamma)$ is the strong elastic scattering of electrons in solids which disturbs the evaluation of electron momenta. Since the mean free path for elastic scattering of electrons in the 10 keV range is a few 10 nm only, very thin target foils are required. As the electron-electron scattering cross section (Mott) is orders of magnitude larger than the photon-electron cross section (Klein-Nishina), $(e,2e)$ experiments can be made with a much better resolution than $(\gamma,e\gamma)$ investigations. On the other hand, multiple electron scattering is more severe in this case since also the projectile is involved in contrast to $(\gamma,e\gamma)$,[23] making intensity (density) interpretation more difficult. As well as obtaining momentum density information, $(e,2e)$ experiments have been successfully used to study energy dispersion of valence bands.[21,25,26] In this sense $(e,2e)$ resembles ARPES, though $(e,2e)$ is not limited to crystals and its interpretation is more straightforward and not hampered by strong transition matrix and interference effects which are particularly important in case of graphite.[5] We also remark that low-energy $(e,2e)$ experiments are being used to investigate aspects of surfaces of crystals.[27–29]

In this paper we report on the EMD of graphite obtained by $(\gamma,e\gamma)$ and $(e,2e)$ experiments. In contrast to earlier investigations,[30,31] the main emphasis of this paper is the study of EMD anisotropies and their comparison with band structure theories. Both experimental techniques obtain results for the EMD. The $(\gamma,e\gamma)$ experiment measures simultaneously the complete 3D-EMD with a rather good momentum resolution, which is used to obtain detailed information about EMD anisotropies for all directions in momentum space. Its crude energy resolution allows only the measurement of the EMD summed over electron states. In contrast, the high momentum and energy resolution of the $(e,2e)$ experiment allows to yield information about state specific EMD and the band structure. No complete 3D-EMD is obtained by the latter method, but additional spectroscopic information is revealed for defined directions in momentum space.

The paper is organized as follows. In Sec. II the methods of the $(\gamma,e\gamma)$ experiment (Sec. IIA) and the $(e,2e)$ experiment (Sec. II B) are presented. In section III the experimental setups for the photon scattering (Sec. III A) and the electron scattering experiment (Sec. III B) are explained. The target preparation and characterization are described in Sec. III C. After a short introduction into the theories used (Sec. IV) experimental results from the $(e,2e)$ (Sec. V A) and the $(\gamma,e\gamma)$ study (Sec. V B) are given and discussed. Finally the results are summarized in Sec. VI.

II. METHOD

Both the $(\gamma,e\gamma)$ and the $(e,2e)$ experiments are very similar. The incoming photon (electron) transfers in a binary collision a large fraction of its energy to a target electron. The target is ionized and the electron leaves the target without further interaction. Thus, as far as the target is concerned, an electron is annihilated at the moment of ionization. The probability that the target is left in a state with energy ε and momentum $\mathbf{p}$ is the spectral function. By measuring the distribution of the pairs of outgoing particles [photon and electron in the case of $(\gamma,e\gamma)$, two electrons in the case of $(e,2e)$] we obtain information about the spectral function as explained next.

A. The $(\gamma,e\gamma)$ experiment

First, we describe the $(\gamma,e\gamma)$ experiment. If a photon with four momentum $\mathsf{k}=(\mathbf{k},\omega/c)$ is scattered at a valence electron with $\mathsf{p}=(\mathbf{p},c-\varepsilon/c)$, where $\varepsilon>0$ is its binding energy, energy and momentum conservation laws demand (we use atomic units, i.e., $\hbar=e=m=1$; in these units the velocity of light is $c=137$ a.u.)

$$\varepsilon(\mathbf{p})=\omega-\omega'-E'+c^2, \tag{2.1a}$$

$$\mathbf{p}=\mathbf{k}'+\mathbf{p}'-\mathbf{k}, \tag{2.1b}$$

where $\mathsf{p}'=(\mathbf{p}',E'/c)$ and $\mathsf{k}'=(\mathbf{k}',\omega'/c)$ are the four momenta of the recoil electron and the scattered photon respectively. Thus, if $\mathbf{k}$, $\mathbf{k}'$ and $\mathbf{p}'$ are known experimentally, $\mathbf{p}$ can be determined in a unique way. For the coincident detection of both the scattered photon and its recoil electron, the triple differential cross section

$$\frac{d^3\sigma}{d\omega' d\Omega_\gamma d\Omega_e}=\frac{1}{2c^4}\frac{\omega' p'}{\omega}X_\gamma(\mathbf{p})\rho(\mathbf{p}) \tag{2.2}$$

holds. The Klein-Nishina cross section function $X_\gamma(\mathbf{p})$ reads in case of linearly polarized photons[32]

$$X_\gamma(\mathbf{p})=\frac{K}{K'}+\frac{K'}{K}+(1-P_1)\left[2c^2\left(\frac{1}{K}-\frac{1}{K'}\right)+c^4\left(\frac{1}{K}-\frac{1}{K'}\right)^2\right] \tag{2.3}$$

with the relativistic invariants

$$K=\mathsf{k}\cdot\mathsf{p}=\frac{E\omega}{c^2}-\mathbf{p}\cdot\mathbf{k}, \tag{2.4a}$$

$$K' = \mathsf{k}' \cdot \mathsf{p} = \frac{E\omega'}{c^2} - \mathbf{p}\cdot\mathbf{k}' = K - \frac{\omega\omega'}{c^2}(1-\cos\theta), \tag{2.4b}$$

where θ is the photon scattering angle. The sign convention of the Stokes parameter P_1 which describes the degree of linear polarization[33] has been chosen so that $P_1<0$ if the $(\mathbf{k},\mathbf{k}')$ scattering plane is identical with the orbital plane of the storage ring. [The $(\gamma,e\gamma)$ experiment has been conducted with synchrotron radiation, see below.] Since our energy resolution does not suffice to resolve specific states, the EMD $\rho(\mathbf{p})$ is summed over all occupied states

$$\rho(\mathbf{p}) = \sum_i \rho_i(\mathbf{p}) \tag{2.5}$$

with

$$\rho_i(\mathbf{p}) = \sum_{\mathbf{k}_c} \left| \int \phi_{\mathbf{k}_c,i}(\mathbf{r}) e^{i\mathbf{p}\cdot\mathbf{r}} d^3\mathbf{r} \right|^2 \Theta[\varepsilon_F - \varepsilon_i(\mathbf{k}_c)]. \tag{2.6}$$

The wave functions $\phi_{\mathbf{k}_c,i}(\mathbf{r})$ are the solutions of the band structure problem for crystal momentum $\mathbf{k}_c = \mathbf{p}+\mathbf{g}$ and band index i. $\mathbf{g}$ is a reciprocal lattice vector which projects $\mathbf{p}$ back to the first Brillouin zone. The $\varepsilon_i(\mathbf{k}_c)$ are the corresponding eigenenergies, ε_F the Fermi energy, and $\Theta(x)$ the step function. Equation (2.2) relies on the validity of the so-called impulse approximation.[22] The dependence of the cross section function $X_\gamma(\mathbf{p})$ on the primary electron momentum is very weak, but it has nevertheless been taken into account when $\rho(\mathbf{p})$ was extracted from the experimental data.

Attempts for a state selective $(\gamma,e\gamma)$ experiment by improvement of the energy resolution especially of the electron branch by a time of flight (TOF) technique have recently been undertaken by Itou *et al.*[34] To reach a time resolution for which the corresponding energy resolution allows at least the separation of the $1s$ state in graphite ($\varepsilon_{1s}=284$ eV), rather low electron recoil energies (12.5 keV) had to be used. This means a strongly enhanced multiple scattering effect due to a reduction of the mean free path for elastic scattering (18 nm). On the other hand, the $1s$ momentum density adds in the momentum region of the valence state an approximately constant contribution of 3% only. Energy resolutions of about 1 eV, which would allow the identification of valence states and which are now feasible in noncoincident Compton spectrometers,[35] seem not to be attainable for $(\gamma,e\gamma)$ experiments in the near future.

B. The $(e,2e)$ experiment

In contrast, the combination of a rather large primary particle flux with a cross section that is orders of magnitude larger than the photon scattering cross section allows $(e,2e)$ experiments to be currently carried out with an energy resolution of about 1 eV, which suffices to evaluate state selective spectral momentum densities (SMD's)

$$\rho_i(\mathbf{p},\varepsilon(\mathbf{p})) = \rho_i(\mathbf{p})\ \delta(\varepsilon(\mathbf{p}) - \varepsilon_i). \tag{2.7}$$

Corresponding to Eqs. (2.1a) and (2.1b), the energy and momentum conservation laws in the case of the $(e,2e)$ experiment give

$$\varepsilon(\mathbf{p}) = E_1 - E_1' - E_2' + c^2, \tag{2.8a}$$

$$\mathbf{p} = \mathbf{p}_1' + \mathbf{p}_2' - \mathbf{p}_1, \tag{2.8b}$$

where $\mathbf{p}_1$, $\mathbf{p}_1'$, and $\mathbf{p}_2'$ are the momenta of the incoming projectile and of the ejected electrons, respectively. The E's are the corresponding total energies. The triple differential cross section for the $(e,2e)$ experiment reads

$$\frac{d^3\sigma_i}{dE'\,d\Omega_1\,d\Omega_2} = 4\frac{p_1' p_2'}{p_1} X_e(\mathbf{p})\ \rho_i(\mathbf{p},\varepsilon(\mathbf{p})) \tag{2.9}$$

with the Mott electron-electron collision factor[36]

$$X_e(\mathbf{p}) = \frac{1}{(\mathbf{p}_1-\mathbf{p}_1')^4} + \frac{1}{(\mathbf{p}_1-\mathbf{p}_2')^4} - \frac{1}{(\mathbf{p}_1-\mathbf{p}_1')^2(\mathbf{p}_1-\mathbf{p}_2')^2}. \tag{2.10}$$

This factor is essentially constant in the noncoplanar symmetric geometry used in the present measurements.

It should be emphasized that both $(e,2e)$ and $(\gamma,e\gamma)$ experiments measure EMD's in the extended zone scheme, i.e., they measure momentum $\mathbf{p}$ and not crystal momentum $\mathbf{k}_c$. This is different from ARPES and ARIPES which are restricted to the momentum range of the first Brillouin zone: the momentum conservation law in case of the photoeffect in a solid is obtained from that of Eq. (2.1b) by replacing $\mathbf{k}'$ with a reciprocal lattice vector $\mathbf{g}$ in such a way that for fixed $\mathbf{k}$ and $\mathbf{p}'$ the primary electron momentum $\mathbf{p}$ belongs to the first Brillouin zone. In contrast to the binary collision experiments described here, photoabsorption has to be supported by the lattice, i.e., with $\mathbf{g}\neq 0$, because otherwise it would be forbidden kinematically: the momentum of the photoelectron had to be zero in the center of mass frame where $\mathbf{k}+\mathbf{p}=0$ holds.

III. EXPERIMENT

A. The $(\gamma,e\gamma)$ experiment

The $(\gamma,e\gamma)$ experiment was performed at the high-energy x-ray undulator beamline of HASYLAB at the 12 GeV PETRA storage ring.[37] The white photon beam was monochromatized by a plane, slightly disordered Si crystal in Laue geometry.[38] The disorder widens the rocking curve considerably compared to the Darwin width of a perfect crystal and matched the monochromaticity of the photon beam (width $\sigma_\omega = 0.35$ keV) with the energy resolution of the photon detector (see below) without a major loss of reflectivity. Thus, a photon flux of 2×10^{12} photons/s in a beam spot of 2×2 mm^2 could be reached at a photon energy of 180.3 keV and an average storage ring current of 30 mA. For photon detection we implemented a two-dimensional array of 12 intrinsic Ge diodes (energy resolution $\sigma_{\omega'} = 0.32$ keV) which was mounted externally to the evacuated target chamber at a scattering angle of $\theta = 150°$ (Fig. 1). The 12-pixel planar

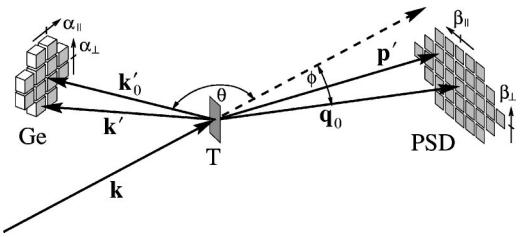

FIG. 1. Experimental (γ,$e\gamma$) setup: Ge, 12-pixel Ge diode; T, target; PSD, 32-pixel position sensitive electron detector.

detector replaces a single diode device with a larger angular acceptance used in earlier investigations.[31] Thus, we improved the transverse momentum resolution significantly compared to the experimental setup with the single diode Ge detector at an identical coincident count rate. The unscattered photon beam was accurately dumped in a lead-shielded hollow body to minimize x-ray background. The electrons were identified by a position sensitive detector (PSD) consisting of a two-dimensional array of 32 individual PIN diodes. The detector arrays were set up in such a way that the vector $\mathbf{q}_0=\mathbf{k}-\mathbf{k}_0'$, i.e., the momentum transfer to an electron initially at rest, was pointing at the center of the PSD, while $\mathbf{k}_0'$, the momentum of the corresponding scattered photon, was defined by the center of the Ge diode array. The surface normal of the target foils was parallel to $\mathbf{q}_0$. The final electron momentum p' is obtained from the energy conservation law of Eq. (2.1a) by neglecting the binding energy ε which is small (tens of eV at most) compared to $\omega_0'=108.7$ keV, where ω_0' is the photon energy after scattering from an electron at rest. A momentum transfer $q_0=75.0$ a.u. guarantees the validity of the impulse approximation. The angle between $\mathbf{q}_0$ and $\mathbf{k}_0'$ (Fig. 1) is $\delta=\theta+\phi=161.2°$. We use a Cartesian coordinate system for the electron momentum $\mathbf{p}$ where the p_z component is parallel to $\mathbf{q}_0$ and the p_x component is lying in the $(\mathbf{k},\mathbf{k}_0')$ scattering plane. In this coordinate system, the initial electron momentum components read

$$p_x=q_0\beta_\parallel-\left(\frac{\omega_0'}{c}\cos\delta\right)\alpha_\parallel+\left(\frac{1}{c}\sin\delta\right)\Delta\omega', \quad (3.1a)$$

$$p_y=q_0\beta_\perp+\frac{\omega_0'}{c}\alpha_\perp, \quad (3.1b)$$

$$p_z=\left(\frac{\omega_0'}{c}\sin\delta\right)\alpha_\parallel-\frac{c\sin\delta}{\omega_0'\sin\theta}\Delta\omega', \quad (3.1c)$$

where $\alpha_{\parallel,\perp}$ and $\beta_{\parallel,\perp}$ are the angular deviations of $\mathbf{k}'$ from $\mathbf{k}_0'$ and $\mathbf{p}'$ from $\mathbf{q}_0$, respectively (Fig. 1), and $\Delta\omega'=\omega'-\omega_0'$ is the photon Doppler broadening. Each detector channel in the photon and electron branch was provided with an independent pre and main amplifier and discriminator. The preamplified photon signals were processed by a spectroscopy amplifier delivering a fast and slow output signal. The discriminated fast signal served as a gate for the coincidence unit, the amplitude of the slow signal was used for the measurement of the final photon energy ω'. If the coincidence unit detected a discriminated electron signal within the open gate, the complete data sets of both the coincidence unit and the ADC were read out via a VME bus.

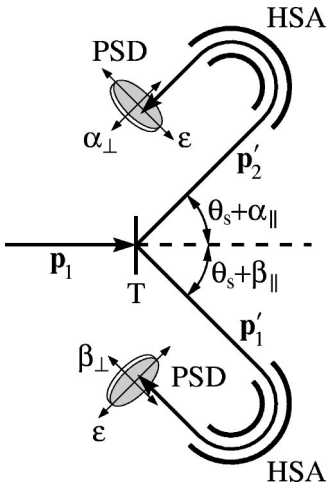

FIG. 2. Experimental (e,$2e$) setup: T, target; HSA, hemispherical electron analyzers; PSD, position sensitive channel plates.

B. The (e,$2e$) experiment

The (e,$2e$) experiment was performed with the new high energy spectrometer developed at ANU.[19] In contrast to earlier arrangement,[20] both detectors for the outgoing electrons are now placed symmetrically at a scattering angle close to $\theta_s=44.45°$. At that angle the cut in the SMD goes through the Γ point, i.e., $\mathbf{p}=0$. This means that for 40 keV primary electrons both emerging electrons have about 20 keV ($p_1'=p_2'=38.7$ a.u.) which is large enough to suppress electron multiple scattering within the target considerably. (It is interesting to note that the deviation $\Delta\theta_s=0.55°$ of the relativistically calculated scattering angle from its nonrelativistic value of 45° for a $\mathbf{p}=0$ measurement results in a momentum deviation parallel to the surface normal of the target foil $\Delta p_\parallel=p_1\Delta\theta_s=0.52$ a.u. which exceeds the experimental uncertainty by far.) The experimental setup is sketched in Fig. 2. The emitted electrons are decelerated and energy analyzed by two hemispherical analyzers. Finally, the electrons are detected by two 2D position sensitive channel plates. For a Cartesian coordinate system, where the p_z component is parallel to $\mathbf{p}_1$, p_x lies in the median scattering plane, and p_y is perpendicular to it, we obtain

$$p_x=p_{10}'\cos\theta_s(\alpha_\parallel-\beta_\parallel)+(2\sin\theta_s)\Delta p_1', \quad (3.2a)$$

$$p_y=p_{10}'(\alpha_\perp+\beta_\perp), \quad (3.2b)$$

$$p_z=p_{10}'\sin\theta_s(\alpha_\parallel+\beta_\parallel). \quad (3.2c)$$

Here $\alpha_\parallel$ and $\beta_\parallel$ are changes in polar angle θ from θ_s which can be selected by deflectors between the specimen and the slits before the analyzers, and $\alpha_\perp$ and $\beta_\perp$ are the azimuthal angles of the detected electrons with respect to the median (horizontal) scattering plane. For ejecting an electron ini-

tially at rest, the scattering angle θ_s (symmetric case) and the final electron momentum $p'_{10}=p'_{20}$ are given by

$$\tan\theta_s=\sqrt{\frac{2c^2}{E_1+c^2}} \qquad \text{and} \qquad p'_{10}=\frac{1}{2c}\sqrt{(E_1+c^2)^2-4c^4}, \tag{3.3}$$

and all three trajectories are in one plane (with $\alpha_\perp=-\beta_\perp$). E_1 is the total primary electron energy and $\Delta p'_1=p'_1-p'_{10}=-\Delta p'_2=p'_{20}-p'_2$ the Doppler broadening term. For our experimental situation the electron pass energy in the hemispherical analyzers is 250 eV corresponding to an energy window of $\Delta E'_1=\Delta E'_2=50$ eV in both analyzers which results in a Doppler broadening $\Delta p'_1=\Delta E'_1/p'_1=0.04$ a.u. that can be neglected. A vertical slit system conforming to $\theta=\theta_s$ in front of the analyzers ensures that coincidence events in horizontal direction of the channel plates are correlated to the binding energy $\varepsilon(p_y)$, whereas those in vertical direction correspond to a 1D cut through the SMD in the p_y direction, i.e., perpendicular to the target surface normal. By adjusting the deflectors in front of these slits to select electrons at angles $\alpha_\parallel,\beta_\parallel\neq 0$, 1D cuts in the p_y direction for fixed values of p_z and p_x can be obtained. For $\alpha_\parallel=\beta_\parallel$ the cuts are with $p_z\neq 0$ and $p_x=0$, for $\alpha_\parallel=-\beta_\parallel$ the cuts are for $p_x\neq 0$ and $p_z=0$. The energy resolution for the binding energy measurement $\varepsilon(p_y)$ is about 1.5 eV [Eq. (2.8a)], the momentum resolution $\Delta p_y\simeq 0.1$ a.u. From Eqs. (2.2) and (2.9) we derive that the triple differential cross section for the $(e,2e)$ experiment is a factor 420 larger than that for the $(\gamma,e\gamma)$ experiment. Together with a beam current of about 1 μA (2×10^{13} electrons/s) this allows for the much improved resolution with, at the same time, a total coincidence count rate of about 1 Hz which is similar to the $(\gamma,e\gamma)$ experiment.

C. The graphite targets

The mean free path for 70 keV recoil electrons in graphite is 90 nm (Ref. 39) [or 25 nm for 20 keV outgoing electrons in case of the $(e,2e)$ experiment], which requires thin target foils to suppress multiple scattering. They were made either by laser plasma ablation (LPA) or by thermal evaporation (TE). In the former case pure graphite was irradiated by a 30 GW/cm^2 Nd:YAG laser for about 10 ns.[40,41] The ablated single C atoms with an average energy of a few eV were collected on a thin betaine film which had a fine crystalline-like structure that acted as a replica for the graphite film and guaranteed a high mechanical stability. For a detailed description of the rather sophisticated preparation of the self-supporting foils we refer to Ref. 42. The TE foils were made by evaporation of graphite heated to about 3200 K. At such moderate temperatures the evaporated species are not monoatomic but carbon clusters of different sizes.[43] These clusters are fragments of the (002) planes and leave the graphite surface with thermal energies of about 0.3 eV.[40] Impinging on the surface of the substrate they do not have sufficient kinetic energy to break the molecular bonds. Again, the evaporated material was condensed on a betaine film which was finally dissolved in water and the self-supporting LPA or TE foils were mounted on a stainless steel frame. The thicknesses of the films were determined by light transmission and were 17 nm for the LPA foil and 18 nm for the TE foil. The mounted foils were finally laser annealed: the TE foil at 4200 K for about 10 ns[44] and the LPA foil for 30 μs at about 3000 K.[41] Transmission electron microscopy revealed a complete graphitezation of the foils and that the average length L_a of the basal planes increased from less than 1 nm immediately after condensation to about 10 nm by this treatment.[44] (Interestingly, it was found by Dollinger *et al.*[41] that heating LPA foils to 4200 K introduces anisotropies in LPA foils by preferential evaporation of oriented C clusters during annealing.) The evaporation time at the relevant vapor pressure ($\approx$10 Pa) of carbon is too low to result in noticeable ablation. Detailed elemental analysis by elastic recoil detection (ERD) showed that the major contamination is a hydrogen coverage of both surfaces of the foils which amounts to an overall content of a few atomic percent.[45]

Foils which had been prepared under identical conditions have extensively been investigated by either high resolution electron microscopy (HREM) or electron diffraction (ED) with 80 keV electrons.[44] While for the LPA foil all low indexed rings of graphite can be observed and their intensity pattern indicates an isotropic distribution of crystallites,[41,44] the (002) ring is missing in case of the TE foil. Since diffraction angles are small for 80 keV electrons ($\Theta_{002}=6.2$ mrad) the lack of this ring implies that (002) planes cannot lie more or less perpendicular to the foil surface. ED patterns from the edge of a folded foil where the surface was nearly parallel to electron beam, developed (002) rings. This clearly demonstrates that for TE foils the basal planes were arranged mostly parallel to the foil surface repeating in essence the results of Klein[46] on evaporated carbon films. The extent of anisotropy was estimated from the azimuthal intensity distribution of the (002) rings and yielded a deviation of the c axis from the foil normal with $\pm 7°$ full width at half maximum (FWHM).[44] Although the $(h\,k\,0)$ and $(0\,0\,l)$-rings of both the LPA and TE foils are identical to those of graphite, there are no $(h\,k\,l)$ rings with h and l or k and l simultaneously nonzero. The same effect can be observed in special cases of bulk graphite (e.g., carbon black,[47,48] often also called ''turbostratic'' graphite[49,50]). This type of graphite consists of parallel (002) planes with almost normal graphite separation,[51] but the planes are shifted and rotated randomly to each other.

As mentioned above, ED of the heat treated LPA foils revealed Debye-Scherrer rings from graphite (sp^2 bonding) and not from diamond (sp^3 bonding). These findings are supported by Díaz *et al.*[52] who report that annealing of LPA foils at temperatures above 1100 K let the sp^3 content fall to zero. It is also interesting to note that recent HREM investigations[53] of thin carbon films made by laser-arc evaporation showed the same dense array of parallel curved graphene sheet segments packed in random orientations as the HREM pictures of Dollinger *et al.*[44] which are representative for our LPA foils. They even show the same tendency to form onionlike graphene arrangements. In addition, the authors of Ref. 53 have supported the sp^2-bonding character of their films by EELS measurements of the π^* peak. The untreated TE foils showed broad ED patterns from which an

average correlation length of about 1 nm was deduced. This low spatial extension led to the interpretation that TE foils are amorphous (a-C) (Ref. 54) though ED shows some anisotropic structure even in the untreated state. We mention that $(e,2e)$ experiments on TE foils[55,56] showed that they consist of trigonally bonded C atoms. These findings are supported by simulations of evaporated *a*-C based on molecular-dynamic methods.[57] It might be worth mentioning that in recent years there has been an overwhelming interest in tetrahedral amorphous carbon (TA-C) due to their huge potential industrial applicability as diamondlike substrates.[58]

In case of the $(e,2e)$ experiment, both TE and LPA foils which had been prepared simultaneously with those for the $(\gamma,e\gamma)$ investigation were measured as is. In the case of the LPA foil we reduced the thickness after an initial measurement to about 5 nm by plasma etching in an Ar-O_2 mixture.[59] A simple glow discharge was used at relatively high pressure (0.5 Torr). Frequently occurring collisions between the ions/molecules ensure that the maximum kinetic energy of the ions is much less than the voltage applied between cathode and anode (300 eV). Etching is thought to occur mainly due to chemical reaction between the carbon foil and oxygen-ions–molecules–atoms in an excited state. In this way, CO and CO_2 are formed and desorb from the surface resulting in a gradual thinning of the film without displacing remaining atoms from their lattice sites. Accordingly, except for a reduction of the multiple scattering background, no change was observed in the spectra. Etching was done in a special preparation chamber from which the foils were transferred to the scattering chamber ($\approx 10^{-10}$ mbar) without breaking the vacuum.

IV. THEORY

Theoretical EMD's are based on either an empirical pseudopotential (PP) method[60] with potential parameters from Reed *et al.*,[61] the full-potential linear muffin-tin orbital (FP-LMTO) (Ref. 62) or the modified augmented plane wave (MAPW) method. All calculations were performed within the general scheme of density functional theory (DFT). In the FP-LMTO method nonoverlapping muffin-tin spheres are introduced and the electron potential and the charge density are expanded in spherical harmonics inside the spheres and Fourier transformed in the interstitial region. In the present calculation 2410 plane waves were used for the representation of the charge density and the potential in the interstitial region. 250 $(\mathbf{k}+\mathbf{g})$ terms were used in the Fourier sums. 77 $\mathbf{k}$ points were produced by division of the irreducible Brillouin zone (BZ). After self-consistency of the electron potential and the charge density had been achieved, the angular averaging (see below) of the EMD was performed. This required calculating the valence band energies and the EMD along 256 directions included within the wedge enclosed by the ΓK, ΓM, and ΓA directions. It is thought that FP-LMTO is superior to the LMTO method within the atomic sphere approximation (ASA).[63] In addition to the problem of overlapping Wigner-Seitz (WS) spheres for the calculation of EMD's,[64] the rather open graphite structure yields discontinuities of the potential at the WS radius which forces the introduction of fictitious empty spheres at interstitial sites.[65] All this is avoided in the FP-LMTO method.

In the MAPW scheme the electron potential is assumed to be of warped-muffin-tin form, e.g., spherical symmetric within the nonoverlapping (APW) spheres centred at each C atom and described by a superposition of plane waves outside the spheres. In the whole atomic cell each Bloch function is expressed by a superposition of up to 364 plane waves and is augmented inside the APW spheres by properly chosen solutions of the radial differential equation with the spherical symmetric potential. Both the wave functions as well as their first derivatives are exactly continuous at the surface of the APW spheres. This guarantees the rapid decay of the Fourier transform of the Bloch functions.[66] The MAPW scheme is an all-electron method which treats the core and valence electron on equal footing. By considering 40 properly chosen $\mathbf{k}$ points in the irreducible BZ, the crystal potential was derived by a self-consistent procedure which was stopped when the first 100 Fourier coefficients of the potential do not change in the first nine digits. Within DFT we considered two different parametrizations of exchange and correlation,[67,68] but found no significant difference in the EMD's. Spherically averaging was performed by generalizing the concept of special directions originally proposed by Bansil in the case of cubic symmetry.[69,70] The evaluation of the basal averaged EMD's was more time consuming as we made a Fourier analysis in cylindrical coordinates with the polar-axis parallel the *c* axis of the crystal and four uniformly spaced angles in the interval $(0,\pi/3)$.

V. EXPERIMENTAL RESULTS AND DISCUSSION

A. The $(e,2e)$ experiment

Both LPA and TE foils have been investigated by the $(e,2e)$ experiment and compared with the $(e,2e)$ measurements of thin HOPG (highly oriented pyrolytic graphite)

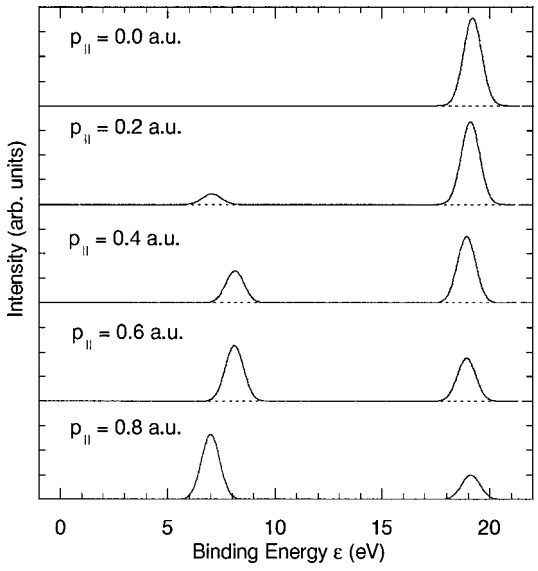

FIG. 3. The azimuthally averaged theoretical SMD (FP-LMTO) as a function of binding energy ε for different $p_\parallel$. The figure holds for $p_\perp = 0$.

films. HOPG consists of a large number of single crystals of graphite, all with their c axis well aligned ($<0.8°$ mosaic spread). It should thus resemble the TE foils. The HOPG film was made from thick material by cleaving followed by plasma thinning. However, the thin area has a diameter of less than 0.5 mm, and these samples are not suitable for $(\gamma,e\gamma)$ spectroscopy since the beam spot exceeds the thin area by far. So first we investigate, using the $(e,2e)$ technique, if the TE and the LPA foil have an electronic structure as suggested by the arrangement of the atoms inferred from the diffraction data, using the HOPG foil as a reference. For this purpose we measured the spectral momentum density for 1D cuts along $p_\perp = p_y$ for $\alpha_\parallel = \beta_\parallel = 0$, i.e., $p_x = p_z = 0$, and also for $\alpha_\parallel = \beta_\parallel = 0.74°$ yielding $p_x = 0$, $p_\parallel = p_z = 0.7$ a.u. [We keep the same nomenclature as for the $(\gamma,e\gamma)$ experiment, i.e., $p_{\parallel,\perp}$ is parallel or perpendicular to the surface normal: for the TE foils and HOPG the c axis is oriented along this surface normal.]

The π band of graphite is formed by $2p$ electrons oriented perpendicular to the basal planes. (We remark that for certain low symmetry directions the terms ''σ or π band'' lose their rigorous meaning since σ_2 and σ_3 bands hybridize with the π band due to their inherent P character.[71]) Hence, these electrons have always a momentum component perpendicular to this plane, as its wave function in momentum space changes sign at $p_\parallel = 0$. Since this band is well separated in energy from the σ band, we can use it to study the anisotropy of the target. Thus, if we tune the spectrometer so it measures momenta with a component $p_\parallel = 0$, then, if the c axis is aligned with the surface normal, we should *not* observe the π band, which has a node and hence zero density in the $p_\parallel = 0$ plane. As a check we used deflectors to tune in to electrons with $p_\parallel = 0.7$ a.u. Now the π band should be observed preferentially in the aligned case.

To illustrate this principle we show in Fig. 3 the calculated spectral momentum density (SMD) of basal averaged graphite using the FP-LMTO approximation as a function of binding energy ε for $p_\perp = 0$ and different $p_\parallel$. The SMD peaks have been broadened by 2 eV to simulate energy resolution and lifetime broadening. It is evident that with increasing $p_\parallel$ the σ intensity (at about 19 eV) decreases on the account of the increasing π intensity (at about 6 eV). Whereas at $p_\parallel = 0$ the π intensity vanishes, it exceeds the σ intensity at $p_\parallel = 0.7$ a.u. Thus, for this point in momentum space, the ratio of π to σ intensity is a sensitive parameter for the degree of c-axis orientation of the foils.

In Fig. 4 the measured intensity plots of the SMD in the $(\varepsilon,p_\perp)$ plane for the reference HOPG foil, the TE and the LPA foil are given. The left side holds for $p_\parallel = 0$, the right

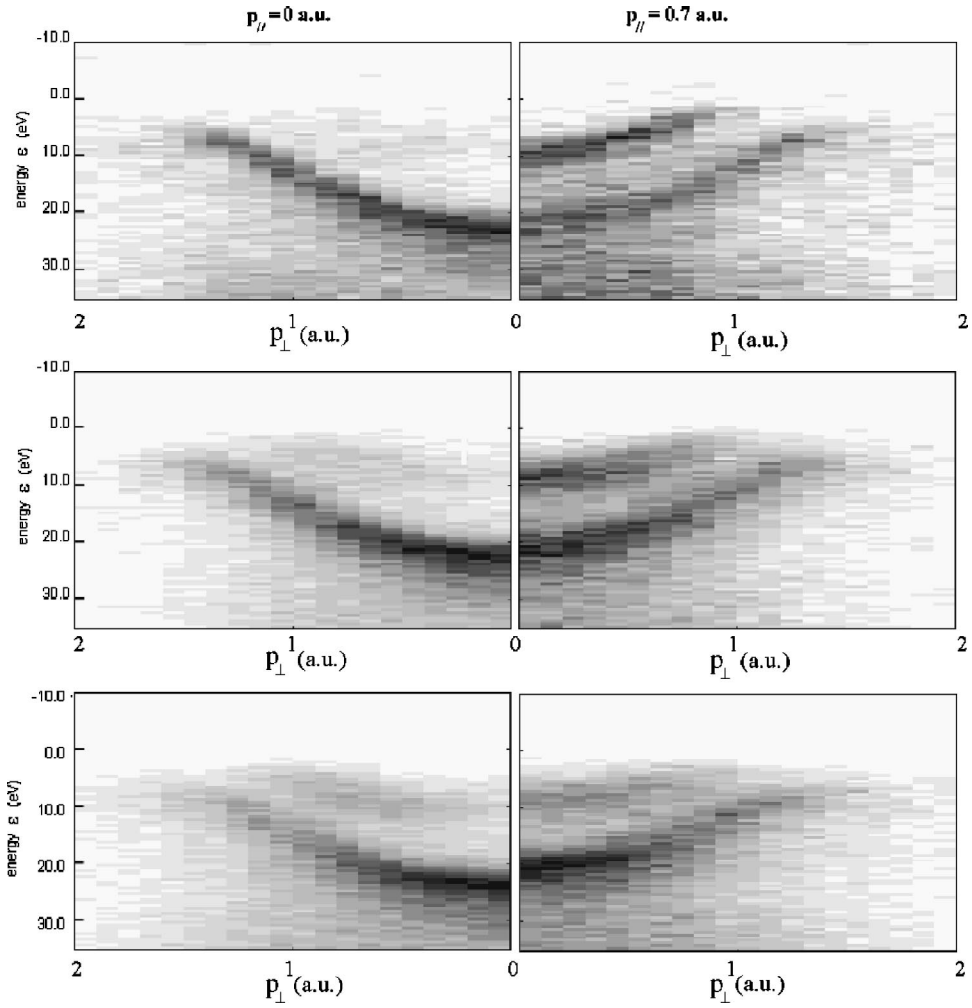

FIG. 4. The experimental SMD from the $(e,2e)$ experiment for different foils as a function of $p_\perp$ at $p_\parallel = 0$ (left) and $p_\parallel = 0.7$ a.u. (right) using a linear grey scale. The top panel is the HOPG foil, the central panel the TE foil, and the LPA foil is displayed at the bottom.

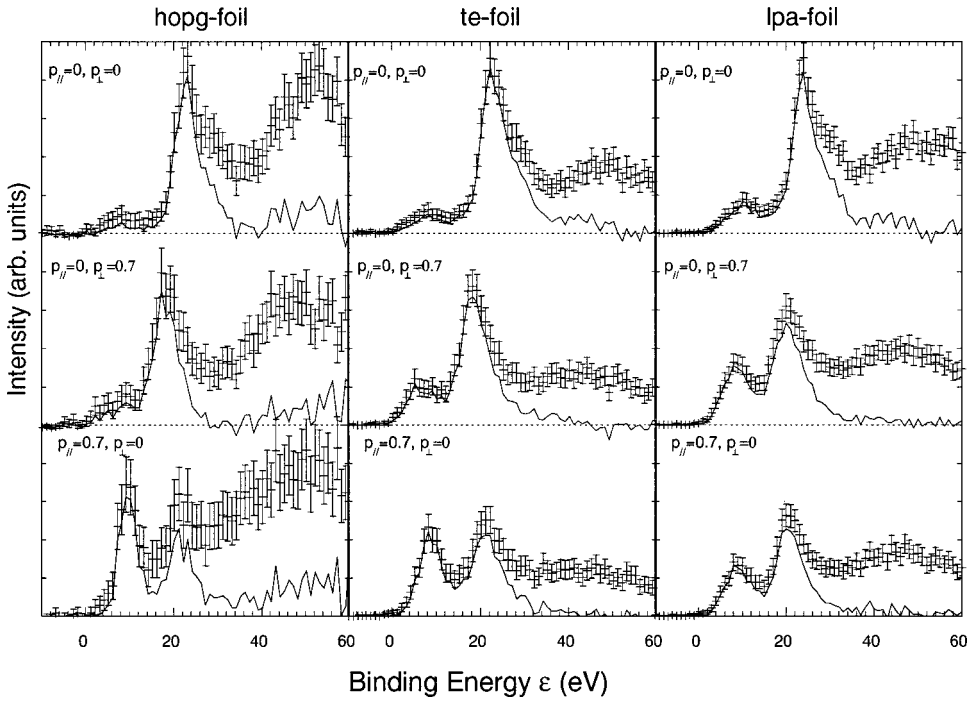

FIG. 5. The measured $(e,2e)$ binding energy spectra for momentum values (in a.u.) as indicated. The left column represents the HOPG sample, the middle column the TE and the right one the LPA foil. The error bars represent the raw data, the full lines are the data after deconvolution for inelastic energy-loss processes.

for $p_\parallel = 0.7$ a.u. For the HOPG film at $p_\parallel = 0$ only σ intensity is observed. The maximum binding energy of this σ band is 26 eV, which is over 6 eV larger than the maximum binding energy of the calculation (19.3 eV, see Fig. 3). This is largely due to the fact that the $(e,2e)$ measurements determine the binding energy relative to the vacuum level and the binding energy scale of the calculation refers to the Fermi level. For $p_\parallel = 0.7$ a.u. both σ and π intensity is found as expected for this foil. The maximum binding energy of the π band is shifted by 6 eV as well. Here, the π intensity exceeds the σ intensity. This is in good agreement with the theoretical prediction of Fig. 3. The TE foil should resemble the HOPG foil. Indeed, the same pattern is observed, although not as clean as for the HOPG film. For $p_\parallel = 0$ the π intensity is weak, but somewhat larger than for HOPG. For $p_\parallel = 0.7$ a.u. the π band is much more pronounced than for $p_\parallel = 0$ but not larger than the σ band. For the LPA foil the π band is observed as a weak feature both for $p_\parallel = 0$ and $p_\parallel = 0.7$ a.u. The LPA foil has more π electrons for $p_\parallel = 0$ than the other foils. The difference in π intensity between $p_\parallel = 0$ and $p_\parallel = 0.7$ a.u. is now much less pronounced.

In order to give a more quantitative impression of the measured intensity we show in Fig. 5 the measured spectra for selected momentum values for the three films. Inelastic scattering (mainly plasmon creation) causes excess intensity at high binding energy. We attempt to correct for this using a deconvolution procedure based on the measured singles electron-energy-loss spectrum.[72] All films were deconvoluted by the same response function, however the deconvoluted amount depends on the film thickness and was adjusted so that the intensity was approximately zero for large binding energies (>40 eV). The deconvoluted intensity is included in Fig. 5 as well. This intensity should be considered more as an educated guess, rather than the result of a rigorously justified procedure. However, the resulting asymmetry in the lineshape with a tail extending from the quasiparticle peak to high binding energy is corroborated by many-body calculations.[73]

Not only the intensity is affected by the presence of *c*-axis orientation in the sample. Energy levels are not expected to disperse as a function of $p_\parallel$ as the different graphite layers are bound together by van der Waals forces rather than covalent bonds. Indeed, the σ binding energy for $p_\parallel = 0$, $p_\perp = 0$ and $p_\parallel = 0.7$ a.u., $p_\perp = 0$ is the same for the HOPG foil and the TE foil, but there is a clear dispersion to lower binding energy with increasing $p_\parallel$ for the LPA foil. For the complete isotropic case, i.e., no preferred *c*-axis orientation, we expect, of course, the same ratio of σ to π intensity for both $p_\parallel = 0$, $p_\perp = 0.7$ a.u. and $p_\parallel = 0.7$ a.u., $p_\perp = 0$. This appears to be the case for the LPA film. Indeed, after normalizing both measurements to the same height, no measurable difference in either peak position or intensity distribution is found for both spectra (Fig. 6). Thus, we conclude that the $(e,2e)$ measurements indicate that the LPA foil displays a spectral function that is isotropic. The TE foil has a preferred *c*-axis orientation along the surface normal, but this orientation is not as well established as in HOPG.

The SMD data are in principle directly comparable with the spectral function of the solid. However, in addition to the finite energy and momentum resolution, multiple scattering effects have to be taken into account. Tracing the peak position as a function of momentum, these data provide information about dispersion, however, for true quantitative comparison we need to take self-energy effects and satellite structures into account as well. For aluminum this approach gives a quantitative description,[74,75] and also for graphite it appears successful.[73] However, within the context of this paper we want to see if we can measure the momentum densities to the extent that the anisotropy in the density is re-

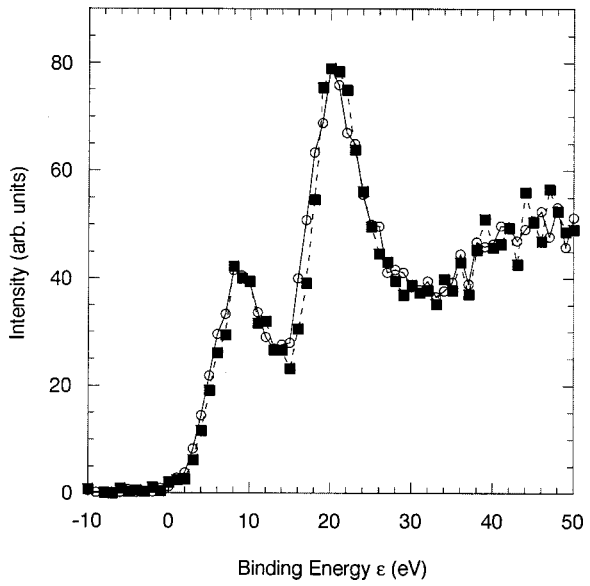

FIG. 6. The measured $(e,2e)$ spectra for the LPA foil at momentum values of $p_{\parallel}=0$, $p_{\perp}=0.7$ a.u. (circles and solid line) and $p_{\parallel}=0.7$ a.u., $p_{\perp}=0$ (squares and dashed line). The spectra are normalized to equal height. The identical shape of these two spectra is expected only for a foil with completely random oriented crystallites.

solved. For this purpose, we consider the extreme cases, the LPA film (random orientation of the c axis) and the HOPG film (well defined c axis).

From the $(e,2e)$ measurement the momentum densities are obtained by energy-integration. However, the measured intensity does not fall to zero above 25 eV binding energy due to both intrinsic and extrinsic satellites. Extrinsic satellites [mainly plasmons created by the incoming and outgoing electrons traveling towards (away) from the $(e,2e)$ collision event itself] are the main cause. Momentum changes associated with plasmons are small, and therefore these plasmon excitations will not affect the momentum density significantly. In order to avoid the problem with the upper integration limit we removed the plasmon contribution by the deconvolution procedure discussed above. It is tempting to try to analyze these spectra in terms of the σ and π electron densities.

The most clearcut analysis would be for the HOPG film. For this purpose we measured an additional set of spectra, under carefully controlled identical experimental conditions for different values of $p_{\parallel}$ using the deflector scheme described earlier. We compare these measurements for the case $p_{\perp}=0$, $p_{\parallel}\neq 0$ with those of Fig. 4 with $p_{\perp}\neq 0$, $p_{\parallel}=0$. The spectra were deconvoluted as in Fig. 5, and subsequently we determined the total area from 0 to 40 eV. This is the (total) $\sigma+\pi$ intensity. The leading edge of the σ band was determined by visual inspection. For the case of $p_{\perp}=0$, $p_{\parallel}\neq 0$, there is no dispersion, so the leading edge position is independent of the momentum value $p_{\parallel}$ measured. For the case of $p_{\perp}\neq 0$, $p_{\parallel}=0$, the leading edge disperses towards lower binding energy with increasing momentum. At the low binding energy side of the leading edge the intensity is called π. The results are plotted in Fig. 7, together with the π and σ

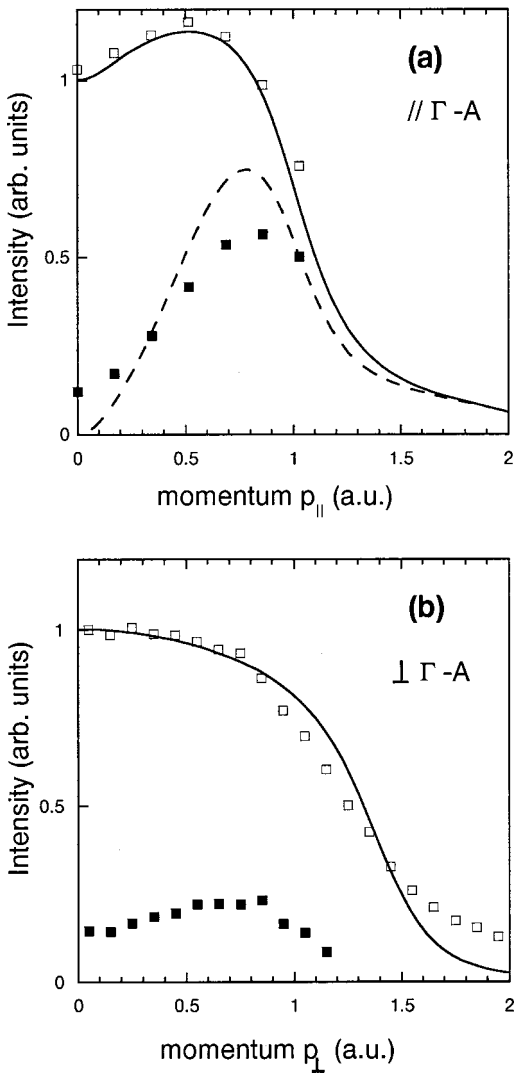

FIG. 7. The total and π-electron momentum density from the $(e,2e)$ experiment for momenta in the ΓA direction (a) and perpendicular to this direction (b). The solid line is the theoretical total density, and the dashed line the corresponding π-electron density. The measured total density and π-electron density are presented by open and filled squares, respectively. All curves refer to FP-LMTO.

intensities obtained from the FP-LMTO calculation. For the first case with the momentum parallel to ΓA the agreement seems reasonable. For the second with the momentum perpendicular to ΓA we should not observe any π intensity. The intensity found is indeed much less. What is seen can only originate from $(e,2e)$ events with additional elastic scattering of either the incident and/or outgoing electrons, and hence with the wrong inferred momentum value. Elastic scattering tends to reduce the observed intensity for momentum values with large densities, and increases the observed intensity for momentum values with low densities, just as is observed for the π-electron density in the ΓA direction. We emphasize that SMD's such as that of Fig. 7 have only been obtained due to the excellent energy resolution of the $(e,2e)$ experiment ($\simeq 1.5$ eV) and are not accessible to the $(\gamma,e\gamma)$ experiment. This holds also for noncoincident Compton scattering where nowadays by use of Bragg spectrometers an

energy resolution of about 1 eV is possible.[35] But as demonstrated by Eisenberger and Platzman[76] Compton profiles are not state specific since due to so-called potential cancellation they are independent of the binding energy ε_i.

Since elastic scattering mixes intensities of SMD's if, in certain areas of momentum space, they overlap in energy, we cannot clearly separate experimentally the σ and π contributions. This problem, however, is avoided for EMD's, i.e., energy integrated SMD's, which we can compare with those obtained from Monte Carlo simulations. In this way we can correct for elastic scattering in a good approximation. Now we want to investigate if we can distinguish between the total momentum distributions of the different foils, and how these compare with theory, using Monte Carlo estimates of the elastic scattering. We consider the measurement done for $p_\parallel = 0$. Integrating this measurement over energy should give us the momentum density as a function of $p_\perp$. Now we can integrate the deconvoluted data and compare it with the theory (FP-LMTO calculation) both for an isotropic and anisotropic case. This is done in Fig. 8. Since the deconvolution procedure accounts for inelastic scattering only, theory has been broadened by a Monte Carlo estimate of the elastic scattering. For that we have studied the influence of elastic multiple scattering on the complete 3D-EMD, and finally 1D cuts of the theory have been made (Fig. 8). Theory has been normalized to experiment at small momenta [Figs. 8(a) and 8(b)], whereas the exact normalization point had negligible influence on the EMD difference of Fig. 8(c). A comparison of Figs. 7(b) and 8(b) demonstrates that the EMD is especially at large momenta strongly influenced by multiple elastic scattering, but after correction for multiple scattering good agreement between theory and experiment is obtained. The MAPW theory yields nearly the same result as FP-LMTO whereas PP predicts a larger EMD at higher momenta if theory is normalized to experiment at small momenta. These findings are in agreement with results from the $(\gamma, e\gamma)$ experiment where a more detailed comparison between the complete 3D-EMD and all three theories will be made (see Sec. V B, Figs. 11 and 13). However, the anisotropy of the momentum distribution [Fig. 8(c)] is rather small both in theory and experiment. This is at first sight quite surprising as experimentally the π band with its characteristic momentum distribution is clearly visible in one case and absent in the other. From band structure calculations we know that the σ density decreases along the ΓA direction by approximately the same amount as the π-intensity increases.[62] Along the ΓM and ΓK directions the π band has no intensity, but the σ band starts decreasing only for momenta with magnitudes slightly larger than the magnitude for which the π band decreases. Thus, the total calculated momentum density profile is quite isotropic. This is found experimentally as well. The main difference in the momentum density of the LPA foil and HOPG for the $p_\perp$ direction is a slightly broader momentum distribution for the planar average, i.e., the HOPG foil. This is to be expected. Due to the large interplanar spacing in graphite, the p electrons perpendicular to the basal planes (which form the π band) will be more extended than those in the basal plane (which contribute to the σ band). As a consequence, the momentum density

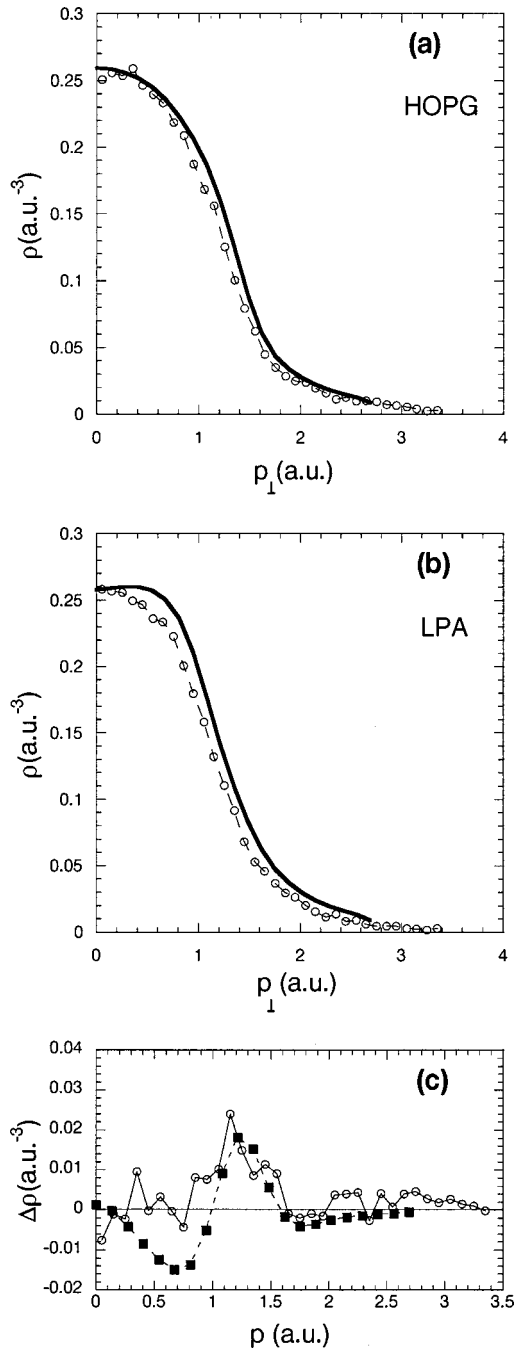

FIG. 8. A comparison between the measured momentum density as obtained from $(e,2e)$ for the HOPG foil and the LPA foil. Also shown, as solid lines, are the theoretical momentum densities of both foils. The theory is corrected for the experimental momentum resolution and elastic multiple scattering. The measured (open circles) and calculated (filled squares) differences are plotted in the lower panel.

will be narrower for the case where the π band contributes (the spherically averaged distribution of the LPA foil) than for the case where the π band is absent (the planar averaged distribution of the HOPG film).

In summary, the SMD results indicate that the momentum density is a much more spherically symmetric object than the spectral function itself. The only significant effect we resolve

is a slightly broader momentum distribution for the planar average (HOPG case), in spite of the fact that before energy integration both measurements are remarkably different. In general, using $(e,2e)$ we have seen that the electronic structure is at least qualitatively as expected from the diffraction data.

B. The $(\gamma,e\gamma)$ experiment

Now we want to explore if the $(\gamma,e\gamma)$ process, which measures the whole of the 3D momentum distribution, can resolve the anisotropy. We will compare experimental $(\gamma,e\gamma)$ results with theoretical expectations from band structure calculations. For this comparison theoretical EMD's have been convoluted with the experimental resolution and corrected for electron multiple scattering. Detailed Monte Carlo (MC) simulations of the momentum resolution $R(p_x,p_y,p_z)$ of the $(\gamma,e\gamma)$ spectrometer included the correlated scattering due to the triple differential cross section of Eq. (2.2), solid angles and energy resolution of both the Ge and PIN diodes, energy broadening of the primary photon beam and the extended beam spot at the target. Since especially the photon energy resolution influences both the p_x and p_z resolution [see Eqs. (3.1a)–3.1c)], they are not independent from each other. The surfaces $R=\text{const}$ are to a good approximation ellipsoids with principal axes which, due to this dependence, are rotated away from the Cartesian coordinate system by a small angle δ.[77] Thus, we fitted a trivariate Gaussian to the MC simulation, and from the diagonal elements of the resulting covariance matrix we obtained the standard deviations $(\sigma_{xx},\sigma_{yy},\sigma_{zz})=(0.14,0.14,0.27)$ a.u. and a nonvanishing off-diagonal element $\sigma_{xz}^2=-7.4\times10^{-3}$ (a.u.)^2 leading to a small anticorrelation. The resolution in p_x and p_y direction is only about a factor of 2 worse than in nowadays high-resolution Compton scattering experiments based on Bragg spectrometers.[78] Whenever in the following the experiment is compared with theory, the latter has been folded with the trivariate Gaussian described above. Emission patterns of the recoiling electrons were recorded by the 2D position sensitive detector with a granularity of about 0.25 a.u. in both p_x and p_y directions. From the thickness of the target foils (about 19 nm) and the mean free path for elastic electron scattering (90 nm) we estimate from Poisson statistics that roughly 90% of the emerging electrons leave the foil without being scattered. [Accidentally, one obtains the same fraction in case of the $(e,2e)$ experiment where the corresponding numbers are 5 nm (thickness) and 25 nm (mean free path).] From the transport cross section of Mayol and Salvat[39] we calculate a rms angle of $\langle\Theta^2\rangle^{1/2}=60$ mrad for a single elastic event. This corresponds to an average momentum uncertainty Δp due to electron scattering by just one event of $\Delta p=q_0\langle\Theta^2\rangle^{1/2}=4.4$ a.u. This estimate demonstrates that electron scattering yields a broad, i.e., nearly constant background of a few percent in the range of 0–3 a.u. Nevertheless, theoretical EMD's have been corrected for this contribution by MC simulations of multiple scattering. Details of this correction can be found in Ref. 79. For comparison with theory experimental data have been normalized to the same integral value as theory in the momentum range $|p_\parallel|=|p_z|\leqslant 2.0$ a.u., $p_\perp=\sqrt{p_x^2+p_y^2}\leqslant 2.0$ a.u., where $p_\parallel$ is parallel to the c axis of graphite and $p_\perp$ lies in the basal plane. Since the position sensitive γ detector consisted of 12 pixels, 12 separate EMD's have been normalized in this way. It should be noted that our experimental conditions allow the measurement of the complete 3D-EMD at once. This is different to the $(e,2e)$ experiment which allows only certain cuts through the EMD, albeit as a function of binding energy. It has also the advantage of determining quite easily the Γ point of the EMD by application of inversion symmetry to the experimental data, i.e., to adjust this point in such a way that $\rho(\mathbf{p})=\rho(-\mathbf{p})$ holds.

In the following part we will compare results of the different calculations with our experimental data, though one should be aware of possible implications due to the special structure of our foils (turbostratic graphite, see above). On the other hand it is well known that both band structure and optical properties of graphite are well reproduced by a single layer (called graphene sheet) calculation.[80–84] Typically, interlayer bonding is attributed to a van der Waals type of dynamic interaction between electrons of adjacent sheets of carbon and amounts to a bond energy of only about 25 meV/atom.[85] A detailed investigation of the electronic structure of turbostratic graphite[49,86] showed that both the band structure and the density of states is essentially the same as that of the Bernal structure except for the immediate vicinity of the Fermi level at the K point which influences especially the transport properties and low-energy excitations such as cyclotron resonance or infrared absorption. We also mention that it is well known that annealing at about 3000 K, which is well below our annealing temperature for the TE foil, converts turbostratic graphite with almost no 3D correlations of layer stacking (Franklin parameter $p\simeq1$)[87,88] into three-dimensional HOPG-like carbon with $p\simeq0$.[51,89] Therefore, a considerable amount of oriented 3D graphite could exist in our foils, and since otherwise both types of foils show comparable shifts and rotations of the (002) planes, we assume that especially the EMD differences are influenced only a little by this structure effect.

Figure 9 shows the calculated valence EMD of graphite either azimuthally [Fig. 9(a)], i.e., in the basal plane, or spherically averaged [Fig. 9(b)]. These EMD's should represent the TE and the LPA foil, respectively. The EMD's are obtained from FP-LMTO approximation. Clearly, theory predicts a bimodal structure of the EMD along the c axis with a saddle point at $p_\perp=p_\parallel=0$ [Fig. 9(a)], resulting from the p character of the π electrons which are responsible for the interlayer bonding. It is this behavior of the EMD which is responsible for the relation $J_\parallel(0)<J_\perp(0)$ for both experimental[16,90,92,93] and theoretical Compton profiles.[94,60,61] An exception on the theoretical side seems to be the Hartree-Fock calculation of Dovesi *et al.*[95] which predicts $J_\parallel(0)>J_\perp(0)$.

In Fig. 10(a) the difference of the theoretical EMD's from Figs. 9(a) and 9(b) is plotted, i.e., basal averaged minus spherically averaged EMD, and Fig. 10(b) shows the influence of resolution and electron multiple scattering on this difference. Evidently, the strength of the anisotropies is reduced, but the general structure is retained. To increase

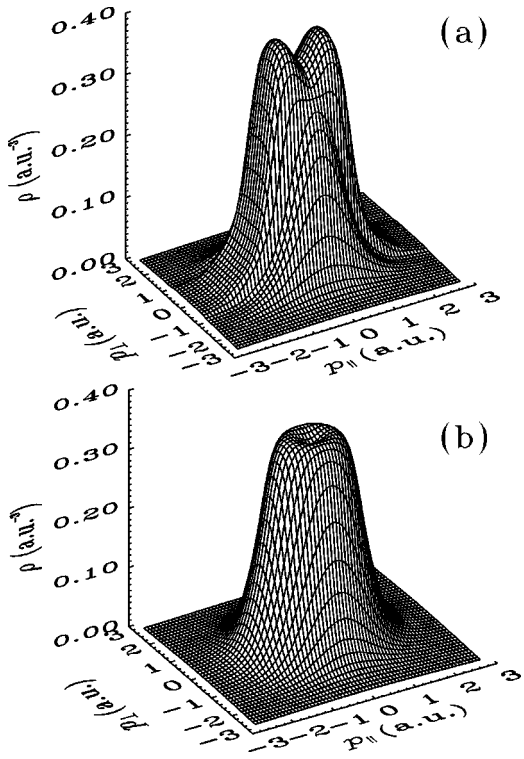

FIG. 9. Azimuthally averaged (a) and spherically averaged (b) electron momentum density of graphite according to FP-LMTO theory.

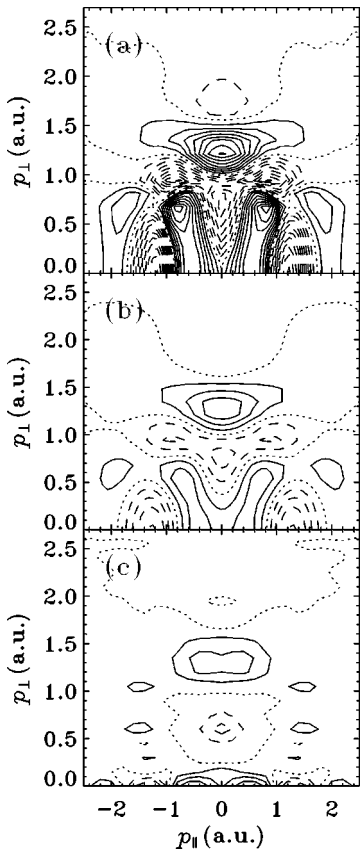

FIG. 10. Contour plot of the difference of azimuthally minus spherically averaged EMD for the $(\gamma,e\gamma)$ experiment. Solid lines hold for a positive difference, dashed lines for a negative one, and the dotted line refers to zero. The theoretical FP-LMTO difference (a), the theoretical difference corrected for experimental resolution and electron multiple scattering (b), and the experimental difference (c). The latter has been symmetrized with respect to $p_\parallel=0$. The difference between the lines is $0.005\,\text{a.u.}^{-3}$ in each case.

statistics, the unbinned data in 3D momentum space from the 12 pixels of the photon detector have been grouped into bins of $\Delta p_\parallel = 0.28$ a.u. and $\Delta p_\perp = 0.15$ a.u. and summed up. This sum and its error have then been divided by the number of photon pixels which contributed to a specific bin. Such a procedure is equivalent to the introduction of a so-called momentum sampling function for binned data well known in positron annihilation and $(e,2e)$ experiments.[96,97] In Fig. 10(c) the experimental difference is plotted and should be compared with the theoretical difference of Fig. 10(b). The comparison reveals that the general features of the experimental anisotropies are reproduced by theory.

For a more quantitative comparison including error bars the following figures show one-dimensional cuts through the EMD's. Figures 11(a) and 11(b) show $\rho(p_\perp, p_\parallel=0)$ for the TE and LPA foils, respectively. Data points are compared with PP (broken curve), FP-LMTO (solid curve), and MAPW (dash-dotted) calculations. Since in all three theories the EMD was obtained by the Fourier transform of the Kohn-Sham pseudo-wave-functions, the so-called Lam-Platzman correction[98] has been applied though its contribution is vanishingly small.[30] Whereas for both the PP and FP-LMTO approximations the azimuthal and spherical average have been obtained by angular integration of the 3D-EMD, in case of the MAPW calculation the special direction method has been applied. Evidently, FP-LMTO and MAPW (with a tendency of MAPW to be superior to FP-LMTO in case of the LPA foil) describe the data better than PP, a fact which has also been recognized by Metz *et al.*[30] (To the valence EMD of Ref. 60 a Roothaan-Hartree-Fock[99] $1s^2$ atomic core has been added.) But we also observe that the often cited deficiency of a PP calculation of not reproducing the wave function oscillations near the nuclei and therefore to underestimate the EMD at large momenta,[94] is not significant for the comparison with our data. The discrepancy between our data and PP is not due to an underestimate of high momentum components—and therefore a reduction of intensity at small momenta due to charge conservation—but due to a different slope of experiment and theory. On the other hand, also noncoincident Compton scattering experiments revealed that PP calculations by Reed *et al.*[61] tend to overestimate momentum anisotropies.[90,92] The sequence of theories if compared with experiment and shown by the 1D cuts of Fig. 11 is also supported by the global fits of the complete 3D-EMD: the normalized χ^2/n (n: number of bins) is 2.15 (MAPW), 3.07 (FP-LMTO), and 3.80 (PP) in case of the TE foil, and 2.22 (MAPW), 2.40 (FP-LMTO), and 2.71 (PP) for the LPA foil. The corresponding normalized standard deviations are in each case ± 0.10. Though there is a clear distinction in the agreement of the three theories with experiment the deviation of the normalized χ^2/n from unity—which would indicate perfect coincidence between theory and ex-

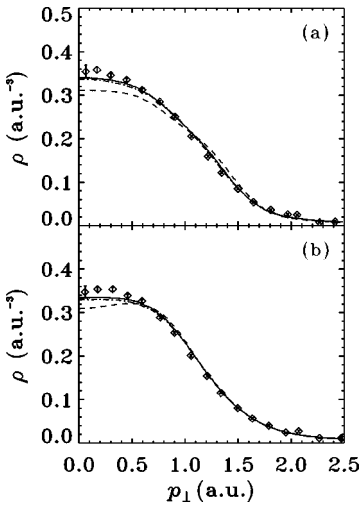

FIG. 11. The EMD from the $(\gamma,e\gamma)$ experiment for the TE (a) and the LPA foil (b) as a function of $p_\perp$ at $p_\parallel=0$. PP: broken line, FP-LMTO: solid line, MAPW: dash-dotted.

periment within the statistical error—is evident. While the visual agreement between theory and experiment in Figs. 11 and 13 seems to be satisfactory the so-called significance level[91] is low, which might be due either to a deficiency of the theories or to a systematic error in our data analysis. Nevertheless we expect that the revealed sequence of theories will not change.

The influence of systematic errors is strongly reduced if differences of the EMD's are considered. In Fig. 12 such differences from TE and LPA foils are plotted as a function of the electron momentum $p_\perp$ in the basal plane for $p_\parallel=0.3$ a.u. [Fig. 12(a)], $p_\parallel=-0.1$ a.u. [Fig. 12(b)], $p_\parallel=-1.0$ a.u. [Fig. 12(c)], and $p_\parallel=-1.4$ a.u. [Fig. 12(d)]. Experimental data are compared again with PP (broken curve), FP-LMTO (solid curve), and MAPW (dash-dotted) calculations. Though the error bars are rather large, the anisotropy is again better described by the FP-LMTO and MAPW calculations rather than the PP one. Since the count rate ΔN for a certain momentum bin $\Delta p_\perp$ increases as $\Delta N\sim p_\perp\Delta p_\perp$, the error bars become smaller with increasing $p_\perp$, which indicates that the maximum of the anisotropy at $p_\perp\simeq 1.3$ a.u. is rather well reproduced by the experiment. (The argument concerning statistics holds strictly for infinitely large detectors only; for finite detectors the sampling probability increases slightly less than proportional to $p_\perp$ and finally even decreases, an effect well known and expressed by the momentum sampling function.)[96,97] The cut at $p_\parallel=-0.1$ a.u. [Fig. 12(b)] should be compared with the $(e,2e)$ result of Fig. 8(c) at $p_\parallel=0$. Whereas the slight minimum at $p_\perp\simeq 0.7$ a.u. predicted by theory is reproduced only by the $(\gamma,e\gamma)$ experiment both experimental techniques agree with theory for the maximum at $p_\perp\simeq 1.3$ a.u.

In Fig. 13 $\rho(p_\perp=0,p_\parallel)$ is compared with theory for the TE foil [Fig. 13(a)] and the LPA foil [Fig. 13(b)]. Whereas the FP-LMTO and MAPW calculations clearly describe the data better at small momenta, PP is slightly superior at larger momenta, though the effect is not strong enough to favor the PP description within the uncertainty of our data. Figure 14

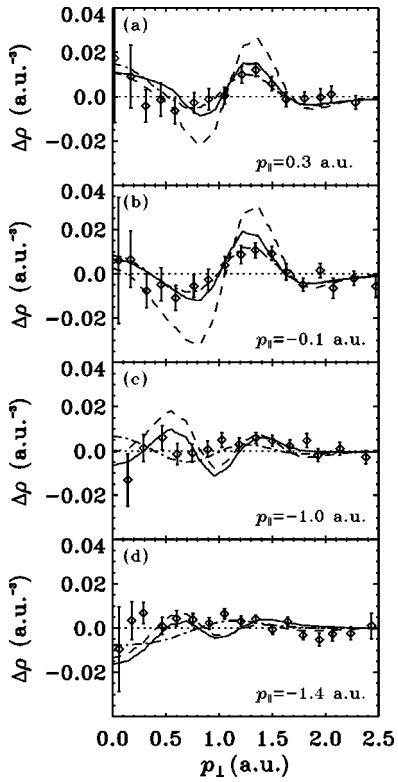

FIG. 12. The difference $\Delta\rho$ of the EMD of the TE foil minus that of the LPA foil as a function of $p_\perp$ for different values of $p_\parallel$. Data points are from the $(\gamma,e\gamma)$ experiment. PP: broken line, FP-LMTO: solid line, MAPW: dash-dotted.

shows the difference of the EMD's from TE and LPA foils $\Delta\rho(p_\perp=\text{const},p_\parallel)$ for $p_\perp=0.0$ a.u. [Fig. 14(a)], $p_\perp=0.9$ a.u. [Fig. 14(b)], $p_\perp=1.3$ a.u. [Fig. 14(c)], and $p_\perp=1.5$ a.u. [Fig. 14(d)]. Though the error bars are rather large, the minimum at $p_\parallel=0$ is better described by FP-LMTO and MAPW than by PP. We mention that in conventional Compton scattering

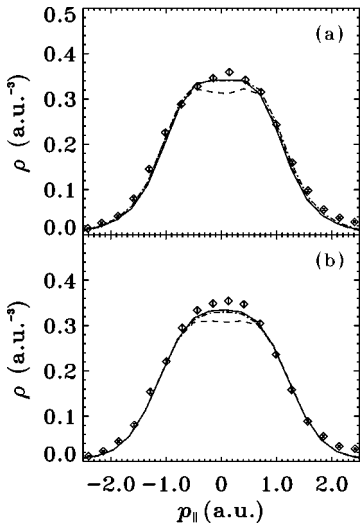

FIG. 13. The EMD from the $(\gamma,e\gamma)$ experiment for the TE (a) and the LPA foil (b) as a function of $p_\parallel$ at $p_\perp=0$. PP: broken line, FP-LMTO: solid line, MAPW: dash-dotted.

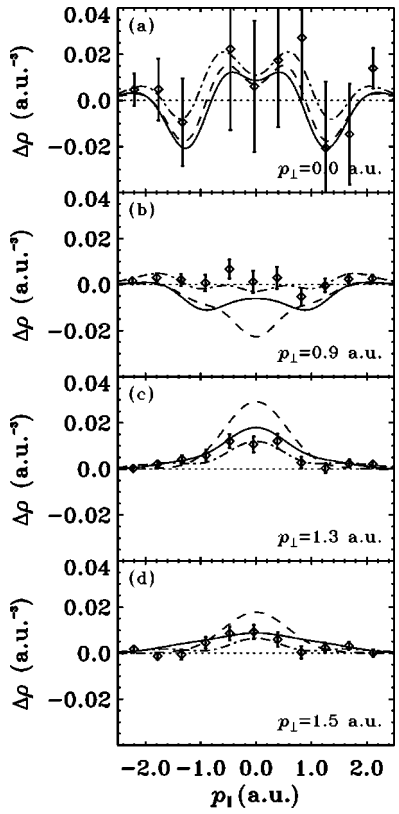

FIG. 14. The difference $\Delta\rho$ of the EMD of the TE foil minus that of the LPA foil as a function of $p_\parallel$ for different values of $p_\perp$. Data points are from the $(\gamma,e\gamma)$ experiment. PP: broken line, FP-LMTO: solid line, MAPW: dash-dotted. In contrast to Fig. 10, the experimental data have not been symmetrized.

work it was also found that PP (Ref. 60) fails to describe the experimental data.[16] It is evident that the theoretical curves are not symmetric with respect to $p_\parallel=0$ which, of course, holds for the EMD. But experimentally, the EMD is measured in $(\Delta\omega',\beta_{\parallel,\perp})$ space instead of $(p_\parallel,p_\perp)$, which means that experimental resolutions and multiple scattering, which are symmetric in $\Delta\omega'$ and $\beta_{\parallel,\perp}$ and connected with momentum space via Eqs. (3.1a)–(3.1c), are asymmetric in $(p_\parallel,p_\perp)$.[77] Finally, we emphasize again that the comparison of experimental data with theory shown in Figs. 11–14 relies on the fitting of the complete 3D-EMD's for each target and not on individual fits for 1D cuts. With regard to the EMD anisotropies discussed above one should be aware of experimental deficiencies which could influence the results: as mentioned in Sec. III c the *c*-axis orientation of the TE foils is not perfect but has an average deviation of $\pm 7°$ FWHM. Though we do not know the exact angular distribution of the *c*-axis model calculations with a Gaussian-like distribution revealed a negligible influence of this effect on the anisotropies. Another error might be that the free-standing foils are not completely flat within the beam spot but wrinkled. This influence is hardly estimated quantitatively but certainly the $(\gamma,e\gamma)$ experiment averages over a larger area (4 mm^2) than the $(e,2e)$ experiment (0.03 mm^2).

VI. SUMMARY AND CONCLUSIONS

The basic idea of a kinematically complete experiment is to measure both the energies and momenta of the free particles contributing to a specific reaction with a target particle in order to reconstruct the unknown properties of the latter in its initial state. In solid state physics this demands momentum uncertainties small compared to the dimensions of the Brillouin zone and an energy resolution better than the Fermi energy. In the context of our experiments this means the simultaneous measurement of all emerging particles with an angular resolution of about 0.1° (to achieve momentum resolution) and an energy resolution of about 1 eV at energies of several tens of keV. This is currently not possible. In the case of $(\gamma,e\gamma)$ experiments the momentum density is determined simultaneously for the complete momentum space with sufficient momentum resolution. However, the energy resolution allows no distinction between valence states. To monochromatize the incoming beam and detect the emerging photons with 1 eV accuracy and an efficiency required for a coincidence experiment is currently not possible. In contrast the $(e,2e)$ experiment has momentum and energy resolution sufficient good to establish details of the band structure and momentum density, but does so only along selected lines in momentum space. Simultaneous measurement of the complete momentum space would require a completely new electron detection scheme. In this sense both techniques are supplementary to each other but allow a comparison where they overlap [Figs. 8(c) and 12(b)].

Specifically, we have measured the 3D electron momentum density and the spectral momentum density—i.e., state sensitive—of thin carbon foils with either isotropically distributed graphitic basal planes or an atomistic structure where the basal planes are parallel to the foil surface. The spectral momentum density has been investigated by the $(e,2e)$ experiment in the equal energy sharing mode. In contrast to the $(\gamma,e\gamma)$ experiment the excellent energy resolution of the $(e,2e)$ experiment ($\approx$1.5 eV) allows a detailed investigation of the graphite band structure and its electron population. The measured intensity of π and σ bands is consistent with the anticipated atomic structure of the targets and is roughly reproduced by either FP-LMTO or MAPW calculations.

The same holds for the results of the $(\gamma,e\gamma)$ experiment where—due to the complete 3D measurement—a more detailed comparison of the EMD anisotropies with theory could be made (Figs. 8 and 14). A comparison of the experimental 3D-EMD with theory yielded a χ^2 based evaluation of theory, where the comparison improves in the order PP, FP-LMTO, MAPW. Naturally, the 3D information about the anisotropy is by far richer than the corresponding difference of noncoincident 1D Compton profiles. Due to the use of 2D-position sensitive detectors for both the electron and the photon branch, counting statistics could be increased considerably within a given beam time which was roughly 72 h for each sample.

We are convinced that similar investigations can be made with other materials, since it is well known that thin monocrystalline films can be prepared by epitaxial growth on

substrates which finally will be dissolved.[100] The general strategy for this kind of experiments in the future is also evident: the measurement of the 3D-SMD with sufficient resolution both in momentum and energy. In case of the $(\gamma,e\gamma)$ experiment this would demand a better photon energy resolution, which in the foreseeable future can only be achieved by Bragg spectrometers. Besides any other problems this would require a brilliance of the primary photon beam which can only be delivered by high lepton energy machines of the fourth generation. In this sense the goal seems to be achievable more easily by the $(e,2e)$ experiment where the primary particle flux is less problematic and the technical challenge of measuring simultaneously the complete 3D-SMD are angle and energy sensitive detectors. On the other hand one should keep in mind that in case of $(e,2e)$ effectively three electrons are sensitive to multiple elastic and inelastic scattering in contrast to the single recoil electron in the $(\gamma,e\gamma)$ experiment.

ACKNOWLEDGMENTS

We are indebted to K. Höppner (University of Dortmund) for help during beam time and C.M. Frey (Technical University of Munich) for the preparation of the carbon foils. We thank Y. Lou (Tsinghua University, Beijing) for the PP calculation of graphite. A.S.K. and M.V. acknowledge support from the Australian Research Council. This work was supported in part by Bundesministerium für Bildung und Forschung, Contract No. 05 ST8HRA.

[1] B.T. Kelly, *Physics of Graphite* (Applied Science, London, 1981).
[2] J.C. Boettger, Phys. Rev. B **55**, 11 202 (1997), and references cited therein.
[3] C. Heske, R. Treusch, F.J. Himpsel, S. Kakar, L.J. Terminello, H.J. Weyer, and E.L. Shirley, Phys. Rev. B **59**, 4680 (1999).
[4] H. Nishimoto, T. Nakatani, T. Matsushita, S. Imada, H. Daimon, and S. Suga, J. Phys.: Condens. Matter **8**, 2715 (1996).
[5] E.L. Shirley, L.J. Terminello, A. Santoni, and F.J. Himpsel, Phys. Rev. B **51**, 13 614 (1995).
[6] F. Maeda, T. Takahashi, H. Ohsawa, S. Suzuki, and H. Suematsu, Phys. Rev. B **37**, 4482 (1988).
[7] I.R. Collins, P.T. Andrews, and A.R. Law, Phys. Rev. B **38**, 13 348 (1988).
[8] J.A. Carlisle, E.L. Shirley, E.A. Hudson, L.J. Terminello, T.A. Callcott, J.J. Jia, D.L. Ederer, R.C.C. Perera, and F.J. Himpsel, Phys. Rev. Lett. **74**, 1234 (1995).
[9] W. Schülke, U. Bonse, N. Nagasawa, A. Kaprolat, and A. Berthold, Phys. Rev. B **38**, 2112 (1988).
[10] J. Kulik, G.D. Lempert, E. Grossman, D. Marton, J.W. Rabalais, and Y. Lifshitz, Phys. Rev. B **52**, 15 812 (1995).
[11] B.M. Kincaid, A.E. Meixner, and P.M. Platzman, Phys. Rev. Lett. **40**, 1296 (1978).
[12] P. Skytt, P. Glans, D.C. Manicini, J.-H. Guo, N. Wassdahl, J. Nordgren, and Y. Ma, Phys. Rev. B **50**, 10 457 (1994).
[13] R. Chen, P. Trucano, and R.F. Stewart, Acta Crystallogr., Sect. A: Cryst. Phys., Diffr., Theor. Gen. Crystallogr. **33**, 823 (1977).
[14] I. Kanazawa, S. Tanigawa, R. Suzuki, M. Sano, and H. Inokuchi, Phys. Rev. B **42**, 11 583 (1990).
[15] R.R. Lee, E.C. von Stetten, M. Hasegawa, and S. Berko, Phys. Rev. Lett. **58**, 2363 (1987).
[16] S. Manninen, V. Honkimäki, and P. Suortti, Z. Naturforsch. A **48**, 295 (1993), and references cited therein.
[17] B.G. Williams and A.J. Bourdillon, J. Phys. C **15**, 6881 (1982).
[18] P. Jonas and P. Schattschneider, J. Phys.: Condens. Matter **5**, 7173 (1993).
[19] M. Vos, G. Kornish, and E. Weigold, Rev. Sci. Instrum. **71**, 3831 (2000).
[20] M. Vos, A. Kheifets, E. Weigold, S.A. Canney, and F.F. Kurp, J. Electron Spectrosc. Relat. Phenom. **87**, 231 (1998).
[21] J.R. Dennison and A.L. Ritter, J. Electron Spectrosc. Relat. Phenom. **77**, 99 (1996), and references cited therein.
[22] C. Metz, Th. Tschentscher, P. Suortti, A.S. Kheifets, D.R. Lun, T. Sattler, J.R. Schneider, and F. Bell, Phys. Rev. B **59**, 10 512 (1999).
[23] F.F. Kurp, M. Vos, Th. Tschentscher, A.S. Kheifets, E. Weigold, J.R. Schneider, and F. Bell, Phys. Rev. B **55**, 5440 (1997).
[24] *Positron Spectroscopy of Solids*, Vol. CXXV of *Proceedings of the International School of Physics ''Enrico Fermi,''* edited by A. Dupasquier and A.P. Mills, Jr. (IOS Press, Amsterdam, 1995).
[25] M. Vos, S.A. Canney, A.S. Kheifets, D.R. Lun, and E. Weigold, J. Phys. IV **9**, 153 (1999).
[26] M. Vos, Z. Fang, S. Canney, A. Kheifets, I.E. McCarthy, and E. Weigold, Phys. Rev. B **56**, 963 (1997).
[27] A. Ruocco, M. Milani, S. Nannarone, and G. Stefani, Phys. Rev. B **59**, 13 359 (1999).
[28] R. Feder, H. Gollisch, D. Meinert, T. Scheunemann, O.M. Artamonov, S.N. Samarin, and J. Kirschner, Phys. Rev. B **58**, 16 418 (1998).
[29] A.S. Kheifets, S. Iacobucci, A. Ruocco, R. Camilloni, and G. Stefani, Phys. Rev. B **57**, 7360 (1998).
[30] C. Metz, Th. Tschentscher, P. Suortti, A.S. Kheifets, D.R. Lun, T. Sattler, J.R. Schneider, and F. Bell, J. Phys.: Condens. Matter **11**, 3933 (1999).
[31] F.F. Kurp, Th. Tschentscher, H. Schulte-Schrepping, J.R. Schneider, and F. Bell, Europhys. Lett. **35**, 61 (1996).
[32] V.B. Berestetskii, E.M. Lifshitz, and L.P. Pitaevskii, *Quantum Electrodynamics* (Pergamon Press, Oxford, 1980).
[33] W.H. McMaster, Rev. Mod. Phys. **33**, 8 (1961).
[34] M. Itou, S. Kishimoto, H. Kawata, M. Ozaki, H. Sakurai, and F. Itoh, J. Phys. Soc. Jpn. **68**, 515 (1999).
[35] K. Hämäläinen, S. Manninen, C.-C. Kao, W. Caliebe, J.B. Hastings, A. Bansil, and S. Kaprzyk, Phys. Rev. B **54**, 5453 (1996).
[36] M. Vos and I.E. McCarthy, J. Electron Spectrosc. Relat. Phenom. **74**, 15 (1995).
[37] U. Hahn, H. Schulte-Schrepping, K. Balewski, J.R. Schneider, P. Ilinski, B. Lai, W. Yun, D. Legnini, and E. Gluskin, J. Synchrotron Radiat. **4**, 1 (1997).
[38] J.R. Schneider, O.D. Gonçalves, A.J. Rollason, U. Bonse, J. Lauer, and W. Zulehner, Nucl. Instrum. Methods Phys. Res. B **29**, 661 (1988).

[39] R. Mayol and F. Salvat, At. Data Nucl. Data Tables **65**, 55 (1997).
[40] G. Dollinger and P. Maier-Komor, Nucl. Instrum. Methods Phys. Res. A **303**, 50 (1991).
[41] G. Dollinger, C.M. Frey, and P. Maier-Komor, Nucl. Instrum. Methods Phys. Res. A **334**, 167 (1993).
[42] P. Maier-Komor, G. Dollinger, C.M. Frey, and H.J. Körner, Nucl. Instrum. Methods Phys. Res. A **362**, 208 (1995).
[43] J. Drowart, R.P. Burns, G. Maria, and G. Inghram, J. Chem. Phys. **31**, 1131 (1959).
[44] G. Dollinger, P. Maier-Komor, and A. Mitwalsky, Nucl. Instrum. Methods Phys. Res. A **303**, 79 (1991).
[45] G. Dollinger, M. Boulouednine, T. Faestermann, and P. Maier-Komor, Nucl. Instrum. Methods Phys. Res. A **334**, 187 (1993).
[46] C.A. Klein, J. Appl. Phys. **33**, 3338 (1962).
[47] J. Biscoe and B.E. Warren, J. Appl. Phys. **13**, 364 (1942).
[48] W. Ruland, in *Chemistry and Physics of Carbon*, edited by P.L. Walker, Jr. (Marcel Dekker, New York, 1968), Vol. 4.
[49] J.-C. Charlier, J.-P. Michenaud, and Ph. Lambin, Phys. Rev. B **46**, 4540 (1992).
[50] H.S. Dresselhaus, G. Dresselhaus, K. Sugihara, I.L. Spain, and H.A. Goldberg, *Graphite Fibers and Filaments*, Vol. 5 of *Springer Series in Materials Science* (Springer, Berlin, 1988).
[51] V. Bayot, L. Piraux, J.-P. Michenaud, J.-P. Issi, M. Lelaurain, and A. Moore, Phys. Rev. B **41**, 11 770 (1990).
[52] J. Díaz, G. Paolicelli, S. Ferrer, and F. Comin, Phys. Rev. B **54**, 8064 (1996).
[53] I. Alexandrou, H.-J. Scheibe, C.J. Kiely, A.J. Papworth, G.A.J. Amaratunga, and B. Schultrich, Phys. Rev. B **54**, 857 (1996).
[54] J. Kakinoki, K. Katada, T. Hanawa, and T. Ino, Acta Crystallogr. **13**, 171 (1960).
[55] C. Gao, Y.Y. Wang, A.L. Ritter, and J.R. Dennison, Phys. Rev. Lett. **62**, 949 (1989).
[56] A.S. Kheifets, J. Lower, K.J. Nygaard, S. Utteridge, M. Vos, E. Weigold, and A.L. Ritter, Phys. Rev. B **49**, 2113 (1994).
[57] R. Galli, R.M. Martin, R. Car, and M. Parinello, Phys. Rev. B **42**, 7470 (1990).
[58] D.R. McKenzie, Rep. Prog. Phys. **59**, 1611 (1996).
[59] M. Vos, P. Storer, S.A. Canney, A.S. Kheifets, I.E. McCarthy, and E. Weigold, Phys. Rev. B **50**, 5635 (1994).
[60] Y. Lou, B. Johansson, and R.M. Nieminen, J. Phys.: Condens. Matter **3**, 1699 (1991).
[61] W.A. Reed, P. Eisenberger, K.C. Pandey, and L.C. Snyder, Phys. Rev. B **10**, 1507 (1974).
[62] A.S. Kheifets, D.R. Lun, and S. Yu Savrasov, J. Phys.: Condens. Matter **11**, 6779 (1999).
[63] H.L. Skriver, *The LMTO Method* (Springer, Berlin, 1984).
[64] A.K. Singh and T. Jarlborg, J. Phys. F: Met. Phys. **15**, 727 (1985).
[65] A.S. Kheifets and M. Vos, J. Phys.: Condens. Matter **7**, 3895 (1995).
[66] H. Roth-Seefried and H. Bross, Z. Phys. B **26**, 125 (1977).
[67] O. Gunnarsson and B.I. Lundqvist, Phys. Rev. B **13**, 4274 (1976).
[68] S.H. Vosko, L. Wilk, and M. Nusair, Can. J. Phys. **58**, 1200 (1981).
[69] A. Bansil, Solid State Commun. **16**, 885 (1975).
[70] W.R. Fehlner, S.B. Nickerson, and S.H. Vosko, Solid State Commun. **19**, 83 (1976).
[71] C. Gao, A.L. Ritter, J.R. Dennison, and N.A.W. Holzwarth, Phys. Rev. B **37**, 3914 (1988).
[72] R. Jones and A.L. Ritter, J. Electron Spectrosc. Relat. Phenom. **40**, 285 (1986).
[73] M. Vos, A.S. Kheifets, E. Weigold, and F. Aryasetiawan, Phys. Rev. B **63**, 33 108 (2001).
[74] S.A. Canney, M. Vos, A.S. Kheifets, N. Clisby, I.E. McCarthy, and E. Weigold, J. Phys.: Condens. Matter **9**, 1931 (1997).
[75] M. Vos, A.S. Kheifets, E. Weigold, S.A. Canney, B. Holm, F. Aryasetiawan, and K. Karlsson, J. Phys.: Condens. Matter **11**, 3645 (1999).
[76] P. Eisenberger and P.M. Platzman, Phys. Rev. A **2**, 415 (1970).
[77] F.F. Kurp, A.E. Werner, J.R. Schneider, Th. Tschentscher, P. Suortti, and F. Bell, Nucl. Instrum. Methods Phys. Res. B **122**, 269 (1997).
[78] P. Suortti, T. Buslaps, P. Fajardo, V. Honkiwäki, M. Kretzschmer, U. Lienert, J.E. McCarthy, M. Renier, A. Shukla, T. Tschentscher, and T. Meinander, J. Synchrotron Radiat. **6**, 69 (1999;); Y. Sakurai, M. Ito, T. Urai, Y. Tanaka, N. Sakai, T. Iwazumi, H. Kawata, M. Ando, and N. Shiotani, Rev. Sci. Instrum. **63**, 1190 (1992); A. Berthold, S. Mourikis, J.R. Schmitz, W. Schülke, and H. Schulte-Schrepping, Nucl. Instrum. Methods Phys. Res. A **317**, 373 (1992).
[79] Th. Tschentscher, J.R. Schneider, and F. Bell, Phys. Rev. B **48**, 16 965 (1993).
[80] F. Bassani and G. Pastori Parravicini, Nuovo Cimento Soc. Ital. Fis., B **50**, 95 (1967).
[81] G.S. Painter and D.E. Ellis, Phys. Rev. B **1**, 4747 (1970).
[82] H. Nagayoshi, K. Nakao, and Y. Uemura, Solid State Commun. **18**, 225 (1976).
[83] R. Dovesi, C. Pisani, and C. Roetti, Int. J. Quantum Chem. **17**, 517 (1980).
[84] A. Zunger, Phys. Rev. B **17**, 626 (1978).
[85] For a recent discussion see M.C. Schabel and J.L. Martins, Phys. Rev. B **46**, 7185 (1992) (the authors attribute interlayer bonding essentially to the overlap of $2p_z$ orbitals); J.-C. Charlier, X. Gonze, and J.P. Michenaud, Europhys. Lett. **28**, 403 (1994).
[86] J.-C. Charlier, X. Gonze, and J.-P. Michenaud, Carbon **32**, 289 (1994).
[87] R.E. Franklin, Acta Crystallogr. **4**, 253 (1951).
[88] W. Ruland, Acta Crystallogr. **18**, 992 (1965).
[89] A.W. Moore, in *Chemistry and Physics of Carbon*, edited by P.L. Walker, Jr. and P.A. Thrower (Marcel Dekker, New York, 1973), Vol. 11.
[90] R. Tyk, J. Felsteiner, I. Gertner, and R. Moreh, Phys. Rev. B **32**, 2625 (1985).
[91] D.E. Groom, F. James, and R. Cousins, Eur. Phys. J. C **15**, 1 (2000).
[92] G. Loupias, J. Chomilier, and D. Guérard, J. Phys. (France) Lett. **45**, L301 (1984).
[93] R.S. Holt, Solid State Commun. **59**, 321 (1986).
[94] M.Y. Chou, M.L. Cohen, and S.G. Louie, Phys. Rev. B **33**, 6619 (1986).
[95] R. Dovesi, C. Pisani, C. Roetti, and P. Dellarole, Phys. Rev. B **24**, 4170 (1981).
[96] R.N. West, in *Positron Spectroscopy of Solids*, Vol. CXXV of *Proceedings of the International School of Physics ''Enrico Fermi,''* edited by A. Dupasquier and A.P. Mills, Jr. (IOS Press, Amsterdam, 1995).

[97] M. Vos, R.S. Caprari, P. Storer, I.E. McCarthy, and E. Weigold, Can. J. Phys. **74**, 829 (1996).
[98] L. Lam and P.M. Platzman, Phys. Rev. B **9**, 5122 (1974).
[99] C.F. Bunge, J.A. Barrientos, and A.V. Bunge, At. Data Nucl. Data Tables **53**, 113 (1993).
[100] *Thin Films and Epitaxy*, Vol. 3 of *Handbook of Crystal Growth*, edited by D.T.J. Hurle (North-Holland Elsevier, Amsterdam, 1994).